


# Guiding of emulsion droplets in microfluidic chips along shallow tracks defined by laser ablation

Zeeshan Rashid<sup>1</sup> · Umut Can Coşkun<sup>2</sup> · Yağız Morova<sup>3</sup> · Berna Morova<sup>3</sup> ·  
Asuman Aşkoğlu Bozkurt<sup>4</sup> · Ahmet Erten<sup>5</sup> · Alexandr Jonáš<sup>3</sup> · Selçuk Aktürk<sup>6</sup> ·  
Alper Kiraz<sup>1,5</sup> 

Received: 3 April 2017 / Accepted: 19 September 2017 / Published online: 23 September 2017  
© Springer-Verlag GmbH Germany 2017

**Abstract** We demonstrate controlled guiding of nanoliter emulsion droplets of polar liquids suspended in oil along shallow hydrophilic tracks fabricated at the base of microchannels located within microfluidic chips. The tracks for droplet guiding are generated by exposing the glass surface of polydimethylsiloxane (PDMS)-coated microscope slides via femtosecond laser ablation. The difference in wettability of glass and PDMS surfaces together with the shallow step-like transverse topographical profile of the ablated tracks allows polar droplets wetting preferentially the glass surface to follow the track. In this study, we investigate guiding of droplets of two different polar liquids (water/ethylene glycol) with and without surfactant suspended in an oil medium along surface tracks of different depths of 1, 1.5, and 2  $\mu\text{m}$ . The results of experiments are also verified with computational fluid dynamics simulations. Guiding of droplets along

the tracks as a function of the droplet composition and size and the surface profile depth is evaluated by analyzing the trajectories of moving droplets with respect to the track central axis, and conditions for stable guiding are identified. The experiments and numerical simulations indicate that while the track topography plays a role in droplet guiding using 1.5- and 2- $\mu\text{m}$  deep tracks, for the case of the smallest track depth of 1  $\mu\text{m}$ , droplet guiding is mainly caused by surface energy modification along the track rather than the presence of a topographical step on the surface. Our results can be exploited to sort passively different microdroplets mixed in the same microfluidic chip, based on their inherent wetting properties, and they can also pave the way for guiding of droplets along reconfigurable tracks defined by surface energy modifications obtained using other external control mechanisms such as electric field or light.

**Electronic supplementary material** The online version of this article (doi:[10.1007/s10404-017-1997-1](https://doi.org/10.1007/s10404-017-1997-1)) contains supplementary material, which is available to authorized users.

✉ Alper Kiraz  
akiraz@ku.edu.tr

<sup>1</sup> Department of Electrical and Electronics Engineering, Koç University, 34450 Sariyer, Istanbul, Turkey

<sup>2</sup> Department of Mechanical Engineering, Istanbul Technical University, 34437 Gümüşsuyu, Istanbul, Turkey

<sup>3</sup> Department of Physics, Istanbul Technical University, 34469 Maslak, Istanbul, Turkey

<sup>4</sup> Department of Physics, Yıldız Technical University, 34220 Esenler, Istanbul, Turkey

<sup>5</sup> Department of Physics, Koç University, 34450 Sariyer, Istanbul, Turkey

<sup>6</sup> Egercili Mahallesi, Gokler Sokak No: 9/2, 55500 Carsamba, Samsun, Turkey

## 1 Introduction

Digital microfluidic systems using chemical microreactors based on isolated liquid droplets represent an attractive platform for carrying out routine reactions and screening tests in clinical, biological, and chemistry laboratories. Since micron-sized droplets have high surface-to-volume ratios, they offer reduced sample requirements and enable rapid mixing of reagents with precision and homogeneity impossible to achieve with conventional macroscopic liquid-dispensing methods, thus allowing new applications in a broad spectrum of analytical and screening assays (Hummer et al. 2016; Rakszewska et al. 2014). When the droplets containing target reagents are placed within an appropriately designed microfluidic chip, a large number of independent operations can be programmed and applied sequentially to each droplet; hence, chemical reactions of interest can

be performed in a highly parallelized, flexible manner at reduced reaction times (Abbyad et al. 2010).

In order to fully exploit the potential of digital microfluidic systems, it is crucial to be able to manipulate selectively individual droplets moving in a continuous stream, as this allows controlled fusion and mixing of the droplet contents and sorting of the droplets on the basis of their chemical composition, size, or mechanical properties. In recent years, several droplet manipulation techniques have been proposed and demonstrated for droplet-based microfluidic systems. In general, these techniques can be divided into two broad classes: active manipulation methods such as optical (Pit et al. 2015), magnetic (Chetouani et al. 2006), acoustic (Franke et al. 2009), and electrokinetic (Ahn et al. 2006) that require a suitable external force to be applied to the target droplet and passive manipulation methods that rely on modifications of the droplet surface energy during its interaction with prepatterned features and structures in the microfluidic environment (Pit et al. 2015).

Active manipulation allows flexible on-demand control of droplets by an external user-controlled mechanism which can reliably and accurately target any selected droplet in the stream. An example of active droplet manipulation is the work by Fradet et al., where laser light was used for localized droplet heating for obtaining surface tension gradients within the droplet surface. Induced Marangoni-type flows then resulted in a “pushing” force repelling the droplet from the laser spot location. In addition, laser light could be used to merge the contents of chemically distinct droplets, thus triggering a chemical reaction of interest (Fradet et al. 2011). Lee et al. controlled the motion of biological cells attached to magnetic beads inside a microfluidic channel via external magnetic field. Because of spatially patterned microscopic magnetic fields produced by a microcoil array, biological cells were trapped and guided actively in microfluidic channel (Lee et al. 2006). Ahn et al. performed active dielectrophoretic manipulation of emulsion droplets using AC electric field created between planar microelectrodes integrated into a microfluidic chip. By turning the AC electric field on and off, they could switch the stream of flowing droplets between collect and waste channels with different hydrodynamic resistances, thus achieving droplet sorting with an effective rate of more than 1.6 kHz (Ahn et al. 2006).

Active manipulation techniques are attractive since they can be combined with the detection of the droplet contents preceding the actual manipulation step. Subsequent manipulation can then be guided by the results of this analysis, thus allowing maximal flexibility in controlling the droplet fate. However, external control and sensing mechanisms increase the complexity and limit the use of such techniques only to sophisticated systems. In contrast, passive manipulation schemes are more straightforward and offer autonomous solutions for microfluidic systems. As a downside, they are

generally fixed and cannot be altered once they are implemented. Passive manipulation can be achieved by creating a gradient of surface interaction energy  $E$  between the droplet and its environment via suitable patterning of the environmental chemical and/or mechanical properties. The presence of such a gradient then results in an effective force that drives the droplet so as to minimize its interaction energy. Typically, this is associated with alternations of the droplet shape which lead to minimization of the overall droplet surface energy  $E = \gamma A$ , where  $\gamma$  is the interfacial tension and  $A$  is the area of interaction surface (Baroud 2014).

Abbyad et al. achieved guiding and trapping of droplet microreactors of nanoliter volumes contained within a thin microchannel (a Hele-Shaw flow cell) by etching patterns into the top surface of the microchannel (Abbyad et al. 2010). Since the height of main flow channel of the cell (35  $\mu\text{m}$ ) was much smaller than the free-droplet diameter of 180  $\mu\text{m}$ , the droplets were forced into a flattened pancake-like shape with big surface area and correspondingly high surface energy. Upon contacting a surface-etched pattern (either a hole or a channel) of depth comparable to the height of the main channel, the droplets entered partially into the hole/channel, thus decreasing their surface area and surface energy. This change of droplet surface energy upon entering the pattern then provided an effective confinement mechanism for droplet guiding and trapping (Dangla et al. 2014). Xu et al. performed fusion and sorting of microdroplets using railroad-like guiding rails. In this demonstration, the droplets were moving along two parallel rails which came closer to each other at the fusion region. At this region, an additional fusion rail started, located symmetrically in the middle between the two original guiding rails. Two droplets moving along the two guiding rails and meeting simultaneously at the fusion region were merged together electrically and guided along the fusion rail toward the fusion outlet. In contrast, droplets arriving at the fusion region individually did not undergo fusion and proceeded to the waste outlets of their corresponding rails. The droplets were squeezed in a 50- $\mu\text{m}$  deep main channel and guided along a 15- $\mu\text{m}$  deep rail (Xu et al. 2012). As compared to the previous work by Abbyad et al., this configuration caused less deformation due to smaller rail depth, resulting in a smaller surface energy modification. Yoon et al. performed passive sorting of droplets using variations in their sizes and/or capillary numbers (Yoon et al. 2014). In their approach, droplets guided along a groove in a Hele-Shaw cell similar to the one used by Abbyad et al. encountered another parallel groove displaced laterally from the original guiding rail. The presence of this additional groove resulted in the appearance of hydrodynamic forces in both axial (along the rail) and transverse (perpendicular to the rail) directions. Depending on the droplet size and surface tension, the transverse hydrodynamic forces could eventually deform the droplet,

overcome the Laplace pressure keeping the droplet in its original rail, and move it to the parallel rail.

Another possibility for guiding emulsion droplets along a solid surface relies on selective patterning of the surface wetting properties. In fact, such controlling of the motion of water droplets along surface heterogeneities is an everyday phenomenon experienced on rainy days on glass windows. This phenomenon has also found many technological applications including cleaning and coating technology. In addition, with carefully designed systems, wetting defects can be externally controlled. As an example of such active control, guiding of conductive water droplets has been demonstrated recently along electrically switchable guides fabricated on an inclined plane (Mannetje et al. 2014).

In this article, we demonstrate passive manipulation and guiding of emulsion droplets of polar liquids suspended in an oil-based host liquid. The droplets are forced to move along wetting and topographical defects represented by hydrophilic tracks obtained by removing thin (thickness: 1–2  $\mu\text{m}$ ) hydrophobic polydimethylsiloxane (PDMS) coatings spun on glass surfaces. Because of the shallow track depths, droplet deformation is much smaller than observed previously (Abbyad et al. 2010; Xu et al. 2012; Yoon et al. 2014; see Fig. 1a for illustration).

In order to obtain the droplet guiding tracks, localized ablation of PDMS layer with focused femtosecond (fs) laser pulses is used. Selective removal of PDMS layer serves two purposes: (a) It exposes hydrophilic glass surface surrounded by hydrophobic PDMS areas, and (b) it generates a topographical feature (a shallow trench) which further forces the droplet to stay within its boundaries. Ablated PDMS-coated glass substrates are then plasma-bonded onto PDMS blocks containing microfluidic channels that are fabricated by standard soft lithography methods. Figure 1a, b provides a schematic diagram of our droplet guiding system.

The height of the main fluidic channel  $h$  is 40  $\mu\text{m}$ , similar to the previously reported works (Abbyad et al. 2010; Xu et al. 2012). In contrast, the depth of the guiding track  $t$  is kept at 1–2  $\mu\text{m}$ , i.e., approximately an order of magnitude smaller than that used by Abbyad et al. Shallow depth of the guiding track used in our experiments increases the relative importance of surface chemistry over surface topography in determining the outcome of the interaction between the droplet and the patterned surface. Experiments performed with two different droplet compositions (water/ethylene glycol) with and without surfactant and the smallest track depth of 1  $\mu\text{m}$  show that droplet guiding is indeed caused mainly by the modification of the channel surface energy along the tracks rather than the presence of topographical steps on the surface.

The paper is organized as follows. In Sect. 2, materials and methods used in the experiments are described together with the numerical model used for computational fluid

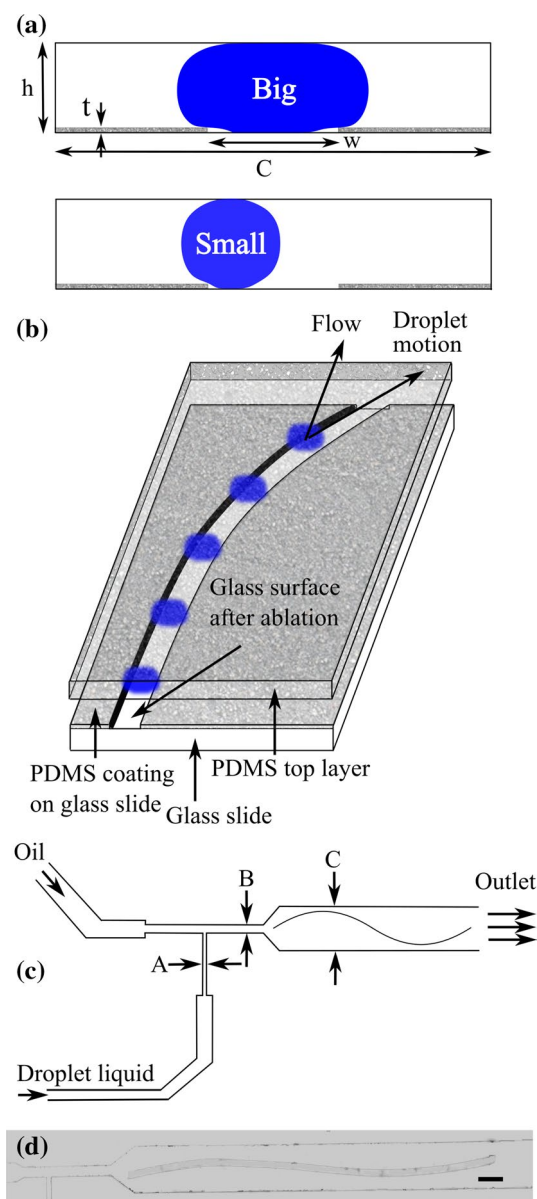


**Fig. 1** Microfluidic chip used in droplet guiding experiments. **a** Illustration of the channel cross section with big (top) and small (bottom) guided droplets.  $C = 400 \mu\text{m}$ ,  $h = 40 \mu\text{m}$ ,  $t = 1\text{--}2 \mu\text{m}$  and  $w = 62.4\text{--}70.8 \mu\text{m}$ . **b** Schematic overall diagram of the chip. **c** Schematic diagram of T-junction device. **d** Snapshot of an actual device. T-junction for the generation of emulsion droplets is visible in the left part of the chip, and the actual guiding track of sinusoidal shape fabricated in the main fluidic channel is visible in the central to right part of the chip. Scale bar: 200  $\mu\text{m}$

dynamics (CFD) calculations. The assumed geometries for droplet generation and guiding in a microfluidic chip and the results of numerical control experiments are also described here. In Sect. 3, results of experiments performed using different guiding track depths and different droplet liquids are described together with their numerical simulations. Finally, conclusions are drawn in Sect. 4.

## 2 Materials and methods

### 2.1 Preparation of microfluidic chips with droplet guiding tracks

Glass slides (dimensions: 76 mm × 26 mm × 1 mm) were initially cleaned by dipping in Hellmanex II (Hellma GmbH & Co.) with 2% concentration in distilled water for 70 min. Hellmanex II is an alkaline liquid detergent which is simply mixed with water to yield an effective cleaning solution for quartz and glass slides. Since the aqueous solution of Hellmanex II reduces significantly the surface tension of water, its good wetting action ensures the efficient removal of dirt particles from the glass surface. At the same time, its high emulsifying and dispersing capabilities prevent the redeposition of the loosened particles. These glass slides were then spin-coated with PDMS (Sylgard 184; Dow Corning) diluted in toluene at different concentrations in order to obtain the desired film thickness (Wang et al. 2011). In particular, three PDMS-to-toluene weight mixing ratios of 1:4, 1:3, and 1:2 were used, producing 1-, 1.5-, and 2- $\mu$ m-thick layers, respectively. PDMS solution was prepared by mixing its base and curing agents at 10:1 weight ratio and then keeping the mixture in vacuum to remove air bubbles. After mixing the PDMS with toluene, cleaned glass slides were spin coated with the mixture at 6000 rpm for 2 min. The coated glass slides were cured in an oven at 75 °C for 2 h.

Droplet guiding tracks were fabricated by laser ablation of the coated glass substrates using a fs-pulsed laser beam (s-Pulse; Amplitude Systemes; Gaussian beam diameter: 1 mm, pulse duration: 550 fs, wavelength: 1030 nm, repetition rate: 1 kHz, and average power: 130 mW). The actual beam power used for ablation could be controlled by a combination of a half-wave plate and a polarizing beam splitter. Precise two-dimensional steering of the beam across the sample necessary for creating the tracks was achieved by a pair of scanning galvo-mirrors. In order to focus the ablation beam on the sample surface, a scan lens with effective focal length of 39 mm (LSM03-VIS; Thorlabs) was placed in the optical path. The beam was sent through the glass substrate and focused at its rear surface that was coated with PDMS. This geometry enables self-focusing of the laser beam within the glass substrate and increases selectivity in removing the PDMS coating without damaging the bulk of the substrate (Jonáš et al. 2014). Approximately 20- $\mu$ m-wide tracks were ablated in a single pass over the surface. By exposing the substrate to the laser beam repeatedly five times, displacing the laser focus by 10  $\mu$ m after each beam pass, ablated channels with a total width of around 60  $\mu$ m could be produced. The actual pattern used for droplet guiding had a sinusoidal shape with peak-to-peak amplitude of 300  $\mu$ m and length of 7 mm (see Fig. 1c, d). After laser ablation, surface profiles of the produced guiding tracks were determined

by a surface profilometer (Dektak 150; Veeco). Exemplary profilometry measurements are shown in Electronic Supplementary Information (ESI) (Fig. S2).

Microfluidic devices based on PDMS elastomer were fabricated using conventional soft lithography technique (Unger et al. 2000). Negative mold of the chip with fluidic channels of height  $h = 40$   $\mu$ m was prepared from SU-8-50 photoresist (Microchem) spin-coated on a silicon wafer. T-junction geometry shown in Fig. 1c was selected for droplet generation. The widths of the channel segments A, B, and C were 50, 100, and 400  $\mu$ m, respectively. After PDMS curing at elevated temperature, PDMS chips and the laser-ablated PDMS-coated microscope slides were exposed to oxygen plasma and the two parts were aligned with each other such that the sinusoidal guiding tracks were centered on the axis of channel section C and then immediately bonded together by firmly joining them. Experimental parameters for the oxygen plasma exposure are summarized in ESI. After bonding, microfluidic devices were kept in an oven at 120 °C for 72 h in order to hasten the recovery of the hydrophobic nature of the PDMS surfaces, required for successful droplet generation (Wu et al. 2008). An actual ablated glass slide bonded with a T-junction chip is shown in Fig. 1d. The pictures of various sections of the T-junction chip were taken by a CCD camera, combined, and subsequently processed to remove background. Here, we report results obtained using three different microfluidic chips. These chips will be referred to as Chip A, Chip B, and Chip C throughout the article. Wetting track depths and track widths for Chips A, B, and C are 1/1.5/2  $\mu$ m and 70.8/62.4/69.3  $\mu$ m, respectively.

### 2.2 Emulsion systems used in droplet guiding experiments

In this article, we study surface-assisted droplet guiding with two different emulsion systems, in particular, polar droplets of (1) water and (2) ethylene glycol with and without surfactant suspended in olive oil serving as the host liquid. Droplets with added surfactant were prepared by mixing sodium dodecyl sulfate (SDS) with either deionized water or pure ethylene glycol to the final SDS concentration of 10 mM which is more than the critical micelle concentrations of SDS in both droplet liquids (Cookey and Obunwo 2015). Thus prepared droplets are called water/SDS and ethylene glycol/SDS droplets throughout this paper. The presence of surfactant in the droplet liquid serves three purposes. Firstly, it makes droplet formation easier. Secondly, it prevents fusion or merging of neighboring droplets flowing in the stream with one another (Tullis et al. 2014). Most importantly, upon adding surfactant, contact angle of water droplets with a glass surface immersed in olive oil increases with respect to the contact angle of pure water on glass in oil. On the other hand, contact angle of ethylene glycol/SDS



droplets with glass immersed in oil does not increase significantly with respect to that of pure ethylene glycol at the same surfactant concentration. This allows us to investigate the effect of contact angle and interfacial tension on the stability of droplet guiding.

In the experiments, olive oil forming the continuous phase of the flow was injected from the top inlet of the chip (see Fig. 1c), using a syringe pump operating at a flow rate of 20 or 30  $\mu\text{L/h}$ . The dispersed (droplet) phase was then injected from the lower inlet of the chip using another syringe pump at a flow rate of 1  $\mu\text{L/h}$ , and emulsion droplets were generated at the T-junction (Garstecki et al. 2006). Subsequently, the droplets entered the channel section C which contained the sinusoidal guiding track.

### 2.3 Computational fluid dynamics study

There are various reasons for conducting numerical simulations of microfluidic experiments. Among the most important motivations are independent verification of experimental results, reduction of the number of experiments and test parameters, and investigation of system configurations whose direct experimental study and evaluation are not feasible. Since the capabilities of numerical simulations have evolved considerably due to the developments in computer science and technology, the number of numerical investigations reported in the literature dealing with modeling of microfluidic devices in chemical and biological engineering applications has increased dramatically in the last few decades (Teh et al. 2008).

The choice of a particular computational method suitable for modeling a specific examined fluid dynamics problem depends heavily on the involved space and timescales that can lie anywhere between subatomic scale to the continuum concept. In this study, the problem of interest is a two-phase flow of immiscible fluids in a microfluidic device; for modeling this class of fluid dynamics problems, the continuum concept and lattice-Boltzmann methods are well suited (Worner 2012). There are many available numerical methods to model such a problem depending on the thickness of the interface between the considered fluid phases. While the arbitrary Lagrangian–Eulerian formulation (Ganesan 2012) and level set methods (Choi and Son 2008) assume zero interface thickness, the phase field (Menech et al. 2008) and the volume of fluid (VOF) (Gupta et al. 2009) methods operate with a continuous interface of finite thickness. In the literature, various flow solvers have been used to tackle such kind of fluid dynamics problems: These include in-house developed source codes (Karapetsas et al. 2016), commercial software such as Ansys Fluent (Gupta et al. 2009) or COMSOL (Lim and Lam 2014), and open-source codes such as OpenFOAM (Malekzadeh and Roohi 2015).

#### 2.3.1 Solver settings

In order to investigate the multi-phase flow of immiscible liquids, Ansys Fluent commercial flow solver based on cell-centered finite-volume computational algorithm was used. To track the interface between the phases, volume of fluid (VOF) method was applied. Continuum surface stress model was selected for modeling surface tension effects. In addition, PISO (Pressure Implicit with Splitting of Operator) algorithm was used for pressure–velocity coupling where the first-order approximations were used for both spatial and temporal discretizations.

#### 2.3.2 Governing equations for fluid flow

VOF method was used to track the shape and position of the interface between the immiscible dispersed and host fluids. In the VOF model, the volume fraction of each fluid in each discrete cell of a fixed mesh is computed and tracked at each time step. Volume fraction  $\alpha$  of each phase can be calculated using the continuity equation given as

$$\frac{\partial}{\partial t}(\alpha_l \rho_l) + \nabla \cdot (\alpha_l \rho_l \vec{u}) = 0 \quad (1)$$

where the subscript  $l$  indicates the phase of interest ( $l = \text{host, dispersed}$ ),  $\alpha_l$  is the volume fraction,  $\rho_l$  is the density, and  $\vec{u}$  is the flow velocity (Ansys Fluent Theory Guide 2013). The right-hand side of Eq. (1) equals to zero since the mass transfer between the phases and mass source terms are absent in our problem. The continuity equation was not directly solved for the host liquid phase; instead, the constraint

$$\alpha_{\text{host}} + \alpha_{\text{dispersed}} = 1 \quad (2)$$

was used to determine the volume fraction of the host liquid  $\alpha_{\text{host}}$  from the calculated volume fraction of the dispersed liquid  $\alpha_{\text{dispersed}}$ .

In order to calculate the velocity field, a single momentum equation was shared by both fluids. This momentum equation in vector form is given as:

$$\frac{\partial}{\partial t}(\rho \vec{u}) + \nabla \cdot (\rho \vec{u} \vec{u}) = -\nabla p + \nabla \cdot [\mu(\nabla \vec{u} + \nabla \vec{u}^T)] + \rho \vec{g} + \vec{F}. \quad (3)$$

Here,  $\rho = \sum_l \alpha_l \rho_l$  is the density of the mixture,  $\mu = \sum_l \alpha_l \mu_l$  is the dynamic viscosity of the mixture ( $l = \text{host, dispersed}$ ),  $p$  is the pressure in the fluid,  $\vec{g}$  is the acceleration due to gravity, and  $\vec{F}$  is the density of all additional volume forces. The solution of Eq. (3) then gives the velocity field  $\vec{u}$  of both phases. From the definition of  $\rho$  and  $\mu$ , it follows that Eq. (3) depends on the volume fraction of each phase through coupled continuity equation Eq. (1) and constraint (2).

### 2.3.3 Computational domain and boundary conditions

The geometry of chips used in the experimental part of the study consisted of a T-Junction followed by a larger channel where a single period of a sine wave-shaped track was ablated into the channel base (see Fig. 1c, d). The main goal of the numerical study was to investigate droplet guiding along the ablated tracks. As the guiding can be observed starting from the beginning of the ablated pattern, only the first quarter of the pattern was included into simulations in order to reduce the computational cost. Figure 2a, b shows a schematic of the computational domain.

Since in the experiments, the droplets are created in a T-junction, most of the flow parameters such as the droplet velocity, droplet diameter, and distance between the droplets are dependent on each other and also on the fluid properties (in particular, fluid viscosity and surface tension). In order to control the flow parameters independently and also to reduce the computational cost, the length of the inlet channel was reduced from 1800 to 600  $\mu\text{m}$  by excluding the first two-thirds of the channel with the T-junction from the simulation domain. Instead of the T-junction, the simulated droplets were generated by changing the inlet volume fraction of the dispersed fluid between 0 and 1 periodically. The desired distance between the neighboring droplets and the droplet size was then controlled by changing the period of the dispersed fluid feed and the duration of the dispersed fluid feed relative to the feed period, respectively.

The whole computational domain was initialized with zero velocity magnitude, water volume fraction, and effective pressure. Constant velocity and constant pressure boundary conditions were applied at the inlet and outlet channel boundaries, respectively. No-slip boundary conditions with experimentally obtained values of contact angles were applied at the walls. Since the T-junction was excluded from the simulation, the inlet velocity was calculated using the total mass flow rate of the host and dispersed fluid. The inlet volume fraction of the dispersed fluid phase was kept at zero for 1 s before the first droplet was sent into the channel by changing the inlet volume fraction to 1.

### 2.3.4 Mesh dependency

In our numerical studies, we investigated the effects of the pattern depth and contact angle of the dispersed fluid with the pattern on the stability of droplet guiding. In order to verify the numerical results and find the proper number and size of the cells that do not lead to computational artifacts, a mesh dependency test was conducted. To this end, we carried out simulations of droplet guiding along a 2- $\mu\text{m}$  deep track using block-structured meshes with different total numbers of cells. In order to capture the

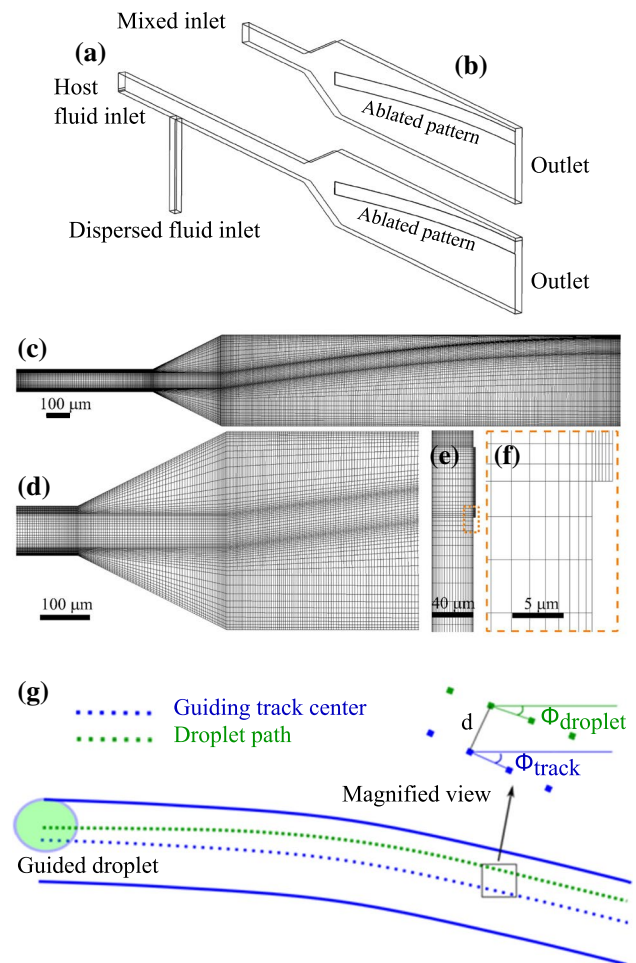


**Fig. 2** Microfluidic chip geometry used in computational fluid dynamics simulations. **a** Full chip including the T-junction and droplet guiding region. **b** Reduced geometry containing only the droplet guiding region. **c** An overall top view of the whole computational domain including the mesh. **d** Detail of the channel expansion region (top view). **e** Side view of the channel outlet. **f** Detailed side view of the region near the track within the area denoted by orange rectangle in part (e). L-shaped mesh domain represents the edge of the guiding track. **g** Schematics showing the droplet trajectory, guiding track center, perpendicular distance  $d$ , and angular analysis of droplet guiding

strong gradients of the flow characteristics, the cells of the mesh were finer near the channel walls, region of expansion from thin to wide channel, and around the sinusoidal guiding track. In these test simulations, we found that a mesh with 2.9 million cells reproduced well the observed experimental results and increasing the number of cells did not lead to further changes in the simulated droplet trajectories. Thus, we used 2.9 million cell mesh in all simulations reported in this article. The actual structure of the mesh is shown in Fig. 2c–f.

### 3 Results and discussion

The results presented and discussed in this article are based on eight sets of experiments performed with different guiding chips and different droplet liquids. Table 1 shows a summary of material parameters and experimental conditions studied in these experiments. In particular, Exps. I–III studying the influence of the track depth on the stability of droplet guiding are introduced in Sect. 3.1, whereas Exps. IV–VIII dealing with the guiding of emulsion droplets formed from different polar liquids are described in Sect. 3.2. Detailed information on the contact angle and interfacial tension measurements is provided in ESI. Normalized cross-correlation-based tracking algorithm has been employed for tracking the positions of moving droplets (see ESI for details). This algorithm has been widely used in the literature for its high efficiency and robustness in tracking moving objects of micrometer size (Sidram and Bhajantri 2015).

#### 3.1 Droplet guiding with different depths of the wetting track

In this subsection we summarize the results of droplet guiding experiments performed with water/SDS droplets in Chips A, B, and C, corresponding to Exps. I, II, and III shown in Table 1, respectively. We also present the results of numerical studies simulating guiding experiments in Chips A and C (Exps. I and III in Table 1).

##### 3.1.1 Droplet guiding experiments

In these experiments, water/SDS droplets of different sizes and speeds were employed. Droplet sizes and speeds ranged between 70–148  $\mu\text{m}$  and 199–244  $\mu\text{m/s}$  for Chip A, 71–146  $\mu\text{m}$  and 193–277  $\mu\text{m/s}$  for Chip B, and 55–151  $\mu\text{m}$  and 215–288  $\mu\text{m/s}$  for Chip C, respectively. Figure 3a–c shows the trajectories obtained by image analysis for all

droplets studied in the particular set of experiments with a single chip. (Corresponding example videos of droplet trajectories can be found in ESI.) Trajectories followed by unguided, partially guided, and completely guided droplets are shown by red, yellow, and green colors, respectively, and the edges of surface-ablated tracks are indicated by blue curves. For each chip, three still images recorded during the motion of an exemplary droplet are also provided. For Chip A with the shallowest track depth of 1  $\mu\text{m}$ , all droplet trajectories are parallel to the walls of the fluidic channel; they follow the direction of the flow and not the ablated track. Hence, none of the droplets are guided for this case. In contrast, for Chip C with the deepest 2- $\mu\text{m}$  track, all the droplets are guided. For the intermediate track depth of 1.5  $\mu\text{m}$  fabricated in Chip B, partial droplet guiding (15 guided out of 31 studied droplets) is observed.

In order to compare quantitatively the stability of guiding for droplets of different sizes, a convention was adopted such that the droplets were divided into three size categories labeled small, medium, and big. For each studied chip, the classification was done so as to yield similar number of droplets in each size category. In particular, small, medium, and big refer to droplet sizes smaller than 90  $\mu\text{m}$  (Chip A)/87  $\mu\text{m}$  (Chip B)/85  $\mu\text{m}$  (Chip C), between 90–110  $\mu\text{m}$  (Chip A)/87–98  $\mu\text{m}$  (Chip B)/85–103  $\mu\text{m}$  (Chip C), and larger than 110  $\mu\text{m}$  (Chip A)/98  $\mu\text{m}$  (Chip B)/103  $\mu\text{m}$  (Chip C), respectively.

Guiding performance of individual chips was then characterized by evaluating the perpendicular distance between the track center and the droplet trajectory and the angular deviation between the track axis and the droplet trajectory for each video frame acquired along the route of the tracked droplet. This was done by comparing each droplet path coordinate with the center of the guiding track in terms of distance ' $d$ ' and angle ' $\Phi$ ' as shown in Fig. 2g.

Coordinates of the  $i$ th point along the droplet trajectory and  $j$ th point along the ablated track center are represented by

**Table 1** Parameters of microfluidic systems used in different sets of droplet guiding experiments

Exp #	Droplet liquid	Track depth ( $\mu\text{m}$ )/chip	Contact angle on PDMS/glass in oil ( $^\circ$ )	Interfacial tension (mN/m)	Droplet size ( $\mu\text{m}$ )	Droplet speed ( $\mu\text{m/s}$ )	Oil/droplet liquid flow rate ( $\mu\text{L/h}$ )	Guiding (yes/no/partial)
I	Water/SDS	1.0/Chip A	163.3/111.2	2.5	70–148	199–244	20/1	No
II	Water/SDS	1.5/Chip B	163.3/111.2	2.5	71–146	193–277	20/1	Partial
III	Water/SDS	2.0/Chip C	163.3/111.2	2.5	55–151	215–288	20/1	Yes
IV	Water/SDS	1.0/Chip A	163.3/111.2	2.5	72–82	267–280	20/1	No
V	Water	1.0/Chip A	171.3/47.7	16.4 (Than et al. 1988)	75–89	394–440	30/1	Yes
VI	Ethylene glycol	1.0/Chip A	164.4/44.4	12.0 (Mei 2008)	96–106	203–245	20/1	Yes
VII	Water	1.0/Chip A	171.3/47.7	16.4	100–117	267–286	20/1	Yes
VIII	Ethylene glycol/SDS	1.0/Chip A	160.8/51.8	–	96–103	228–265	20/1	Yes

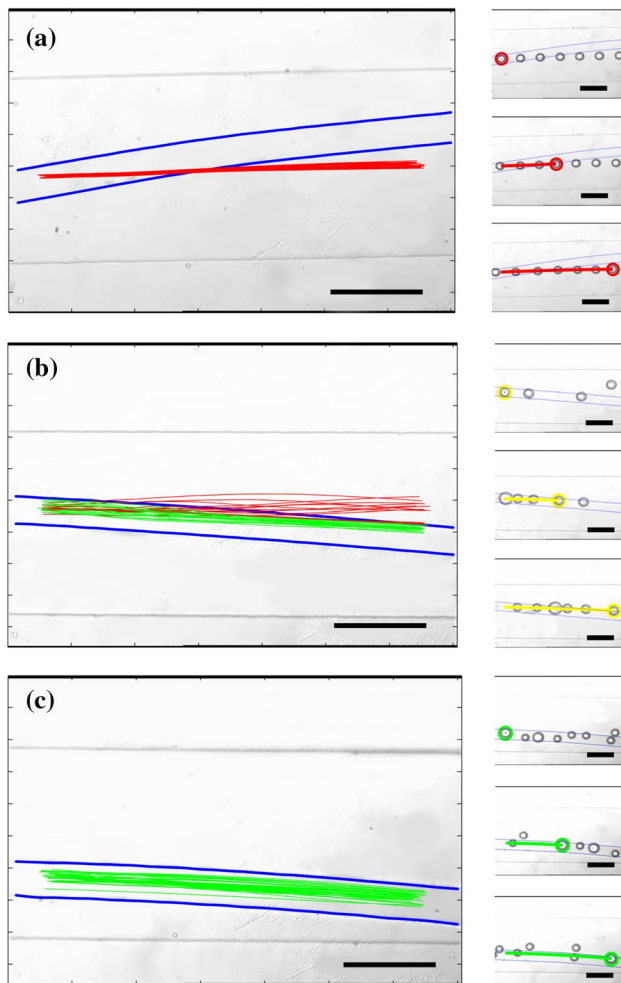


**Fig. 3** Droplet guiding as a function of the track depth. Experimental trajectories observed for water/SDS droplets in **a** Chip A with 1  $\mu\text{m}$  depth, **b** Chip B with 1.5  $\mu\text{m}$  depth, **c** Chip C with 2.0  $\mu\text{m}$  depth, (Exps. I, II, and III, respectively). Red, green, and yellow lines represent unguided, guided, and partially guided (guided or unguided) droplet trajectories, respectively, and blue lines represent boundaries of the guiding track. Droplet guiding movies of these experiments can be seen in ESI (Movies S1, S2, and S3, respectively). All scale bars are 200  $\mu\text{m}$

$(r_{i,x}, r_{i,y})$  and  $(s_{j,x}, s_{j,y})$ , respectively. Here, subscripts  $x$  and  $y$  refer to the horizontal and vertical directions in a two-dimensional image, respectively. For each position  $(r_{i,x}, r_{i,y})$  along the droplet trajectory, the corresponding position  $(s_{j,x}, s_{j,y})$  on the track center was found that minimizes the perpendicular distance  $d_i$  between the droplet trajectory and the track center.  $j$  indicates the index number along the ablated track center minimizing the distance with the  $i$ th point along the droplet trajectory. The value of  $d_i$  is then given by:

$$d_i = \sqrt{(r_{i,x} - s_{j,x})^2 + (r_{i,y} - s_{j,y})^2}. \quad (4)$$

Local directions of the droplet trajectory at point  $(r_{i,x}, r_{i,y})$  and of the center of the ablated track at point  $(s_{j,x}, s_{j,y})$  with respect to the channel side walls are characterized by angles  $\Phi_{\text{droplet},i}$ ,  $\Phi_{\text{track},j}$  defined as:

$$\Phi_{\text{droplet},i} = \arctan \left[ \frac{r_{(i+1),y} - r_{i,y}}{r_{(i+1),x} - r_{i,x}} \right], \quad (5a)$$

$$\Phi_{\text{track},j} = \arctan \left[ \frac{s_{(j+1),y} - s_{j,y}}{s_{(j+1),x} - s_{j,x}} \right], \quad (5b)$$

Angular deviation between the droplet trajectory and the track center at a given pixel is then obtained as:

$$\Delta\Phi_i = |\Phi_{\text{droplet},i} - \Phi_{\text{track},j}|. \quad (6)$$

The same analysis is done for all the droplets, and the results are combined to evaluate the overall quality of guiding for the studied system. The values of  $d_i$  and  $\Delta\Phi_i$  obtained for all trajectory points of all droplets within individual chips have been combined and are shown as histograms in Fig. 4. The distance histograms reveal the confinement of the droplets within the track, while the angle histograms reveal their guiding.

The results obtained for Chip A (track depth: 1  $\mu\text{m}$ ), plotted in Fig. 4a, d, clearly show that droplets of all sizes are neither confined in the track nor following the track direction. All distance histograms of Fig. 4a are virtually flat, indicating no fixed separation between the track axis and the droplet center. In addition, the angle histograms of Fig. 4d are also quite broad, reflecting a wide range of angles between the droplet trajectory and the track axis that is parallel to the sinusoidal contour of the track. This stems from the fact that the droplets are moving predominantly in the direction of the flow, ignoring the presence of the ablated track. Overall, the data show no guiding for Chip A, which results from insufficient depth of the ablated track.

The histograms plotted in Fig. 4b, e correspond to Chip B (track depth: 1.5  $\mu\text{m}$ ). In this case, due to the interplay between the flow direction and position of the topographical step, guided droplets tend to stay away from the center of the guiding track and follow its downstream edge. Therefore, all the distance histograms of Fig. 4b peak at nonzero positive values of  $d$ . However, the average separation distance  $\bar{d}$  between the track axis and the droplet center visibly decreases with increasing droplet size. Since Chip B only enables partial droplet guiding, the effect of droplet size is not too pronounced because the droplets are confined only loosely within the track. Despite this, the angle histograms of Fig. 4e are shifted to significantly smaller values relative to the data obtained with Chip A (compare with Fig. 4d), thus showing better guiding caused by a deeper track.



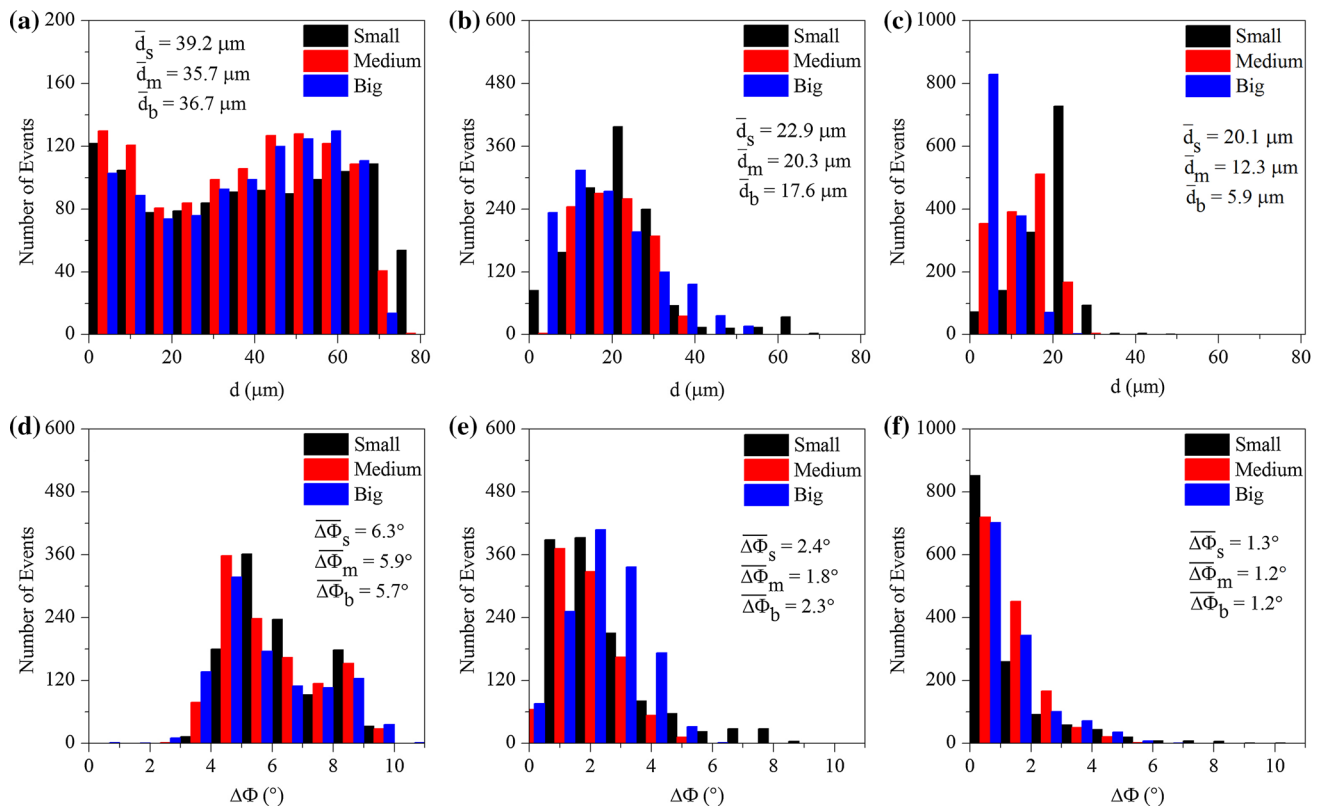


**Fig. 4** Guiding performance of surface-ablated tracks of different depths. **a–c** Distance histograms observed for Chips A, B, and C for different droplet size groups. **d–f** Angular deviation histograms observed for Chips A, B, and C for different droplet size groups.

Mean values of the separation distances and angular deviations for different droplet size groups are indicated in figure legends. Total numbers of small/medium/big droplets studied are 10/10/10 for Chip A, 11/9/11 for Chip B, and 14/16/15 for Chip C

Finally, the histograms plotted in Fig. 4c, f correspond to Chip C (track depth: 2  $\mu\text{m}$ ). Similarly to the previous case of Chip B, small droplets tend to stay near the track edge so that the peak of their distance histogram shown in Fig. 4c (black bars) is located at a relatively large value of  $d$ . However, with increasing droplet size, the peaks of the distance histograms shift strongly toward the zero value of  $d$ . Because the droplet confinement is almost complete for this case, the effect of droplet size is much more pronounced than for Chip B. As seen in the angular deviation histograms of Fig. 4f, Chip C enables almost perfect guiding of droplets of all sizes. Thus, the peaks of the angular deviation histograms have all shifted toward the zero value of  $\Delta\Phi$ .

### 3.1.2 Numerical simulations of droplet guiding

In order to gain more insight into the mechanisms of droplet guiding, the effect of ablated region depth has been investigated numerically. In this CFD study, the depth of the sinusoidal guiding pattern was chosen to be either 1 or 2  $\mu\text{m}$ , corresponding to the two extreme experimental cases of Chip A and Chip C (Exps. I and III in Table 1). We assumed that the guiding track was formed by a clean glass surface,

whereas the region surrounding the track was formed by PDMS surface. Both surfaces were characterized by their static contact angles which were determined experimentally for droplets of water/SDS mixture immersed in olive oil. In addition, dynamic behavior of immiscible fluids in the two-phase flow was described by their interfacial tension which was measured for an interface between water/SDS and olive oil by the Wilhelmy plate method as in Aas et al. (2013). The details of contact angle and interfacial tension measurements are provided in ESI. Measured interfacial tension and contact angles are summarized in Table 1; these values were applied in the simulations in order to make them as realistic as possible. In all numerical results presented in the article, droplet colors indicate different fluids where red, green, and blue colors are used for water/SDS, pure water, and pure ethylene glycol, respectively.

The simulations of droplet guiding yielded video files showing water/SDS droplets flowing in oil toward the channel outlet; these video files can be found in ESI (movies S9 and S10). The last frames of the simulated videos produced for 1- $\mu\text{m}$  and 2- $\mu\text{m}$  deep tracks, with six droplets present simultaneously in the channel, are shown in Fig. 5a, b, respectively. It is evident that majority of the droplets are

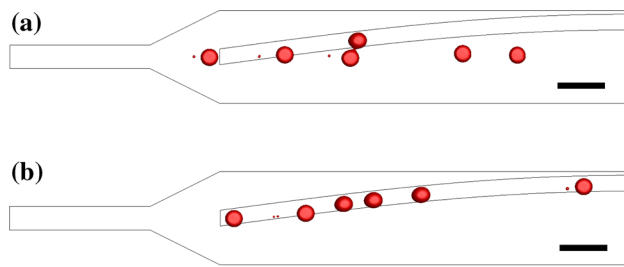


**Fig. 5** Numerical simulation of guiding of water/SDS droplets in **a** Chip A (track depth: 1  $\mu\text{m}$ ) and **b** Chip C (track depth: 2  $\mu\text{m}$ ) corresponding to Exps. I and III. See also Movies S9 and S10 in ESI. All scale bars are 200  $\mu\text{m}$

not guided for the shallow track (Fig. 5a), whereas all the droplets moving along the deep track are guided (Fig. 5b).

### 3.2 Droplet guiding with different droplet liquids

In this subsection, we present the results of Exps. IV–VIII described in Table 1, obtained using Chip A and two different droplet liquids with different wetting properties on the glass surface immersed in oil. In particular, the studied liquids include water and ethylene glycol, both used either with or without surfactant. In addition, the results of numerical studies performed for parameters corresponding to Exps. IV–VII are also presented here. All the parameters relevant to experimental and numerical studies IV–VIII are summarized in Table 1.

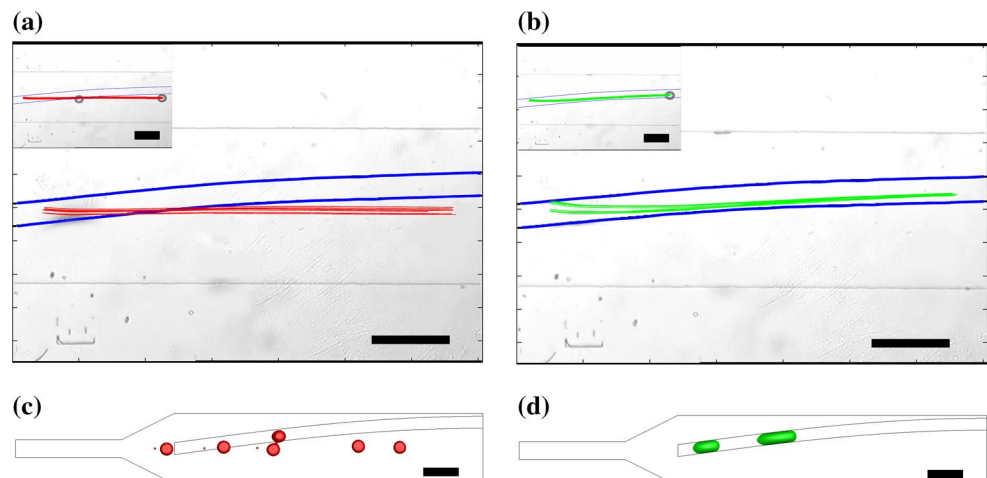
Contact angles measured for all studied droplet liquids on PDMS and glass surfaces immersed in olive oil are shown in Table 1. On the PDMS surface, contact angles for pure water and pure ethylene glycol were found to be  $171.3^\circ$  and  $164.4^\circ$ , respectively. These values are similar to the contact angles measured on PDMS for water/SDS droplets ( $163.3^\circ$ ) and ethylene glycol/SDS droplets ( $160.8^\circ$ ). The difference between contact angles of individual liquids becomes much

more prominent when the surface is changed to glass. On the glass surface, contact angles were measured to be  $47.7^\circ$ ,  $44.4^\circ$ ,  $111.2^\circ$ , and  $51.8^\circ$  for pure water, pure ethylene glycol, water/SDS, and ethylene glycol/SDS droplets, respectively. Consequently, the contrast between the contact angles measured on PDMS and on glass is much smaller for water/SDS droplets, in comparison with water, ethylene glycol, and ethylene glycol/SDS droplets.

Experimental and simulated trajectories determined for water/SDS and pure water droplets in Chip A (Exps. IV and V) are shown in Fig. 6. In order to obtain similar droplet sizes in both experiments, oil flow rate of  $30 \mu\text{L/h}$  was used in Exp. V with pure water droplets, whereas in Exp. IV with water/SDS droplets, oil flow rate was kept at  $20 \mu\text{L/h}$ . This difference in the applied flow rates is due to almost seven-fold difference in interfacial tensions for both cases. Consequently, the droplet speed in Exp. V is considerably higher than the droplet speed in Exp. IV because the size and speed of moving droplets are interrelated (Garstecki et al. 2006). In particular, for the data presented in Fig. 6a, droplet size and speed ranged from  $72\text{--}82 \mu\text{m}$  to  $267\text{--}280 \mu\text{m/s}$ , respectively. In contrast, for the data presented in Fig. 6b, droplet size and speed ranged from  $75\text{--}89 \mu\text{m}$  to  $394\text{--}440 \mu\text{m/s}$ , respectively. Despite the higher droplet speeds, all droplets are observed to be guided in Exp. V (water), while in Exp. IV (water/SDS), no single droplet is guided.

From the comparison of Exp. IV (water/SDS) and V (water), we conclude that the main mechanism enabling droplet guiding is the modification of interfacial energy between the droplet surface and the surface of the guiding track rather than the topography of the track. In other words, due to a higher contrast of contact angles between the PDMS and glass surfaces for pure water droplets as compared to water/SDS droplets (see Table 1), pure water droplets are much more strongly attracted to the laser-ablated track. These experimental results have also been verified by numerical simulations whose outcome is shown

**Fig. 6** Droplet guiding experiments performed with **a** water/SDS and **b** pure water droplets in Chip A (Exps. IV and V). Parts **c** and **d** show the simulation results for the experiments presented in parts **a** and **b**, respectively. Droplet spreading in part **d** of the figure results from the low contact angle of pure water on the clean glass surface which is actually not achieved in the experiments (see discussion in the text.) All scale bars are 200  $\mu\text{m}$ . See also Movies S4, S5, S9, and S11 in ESI



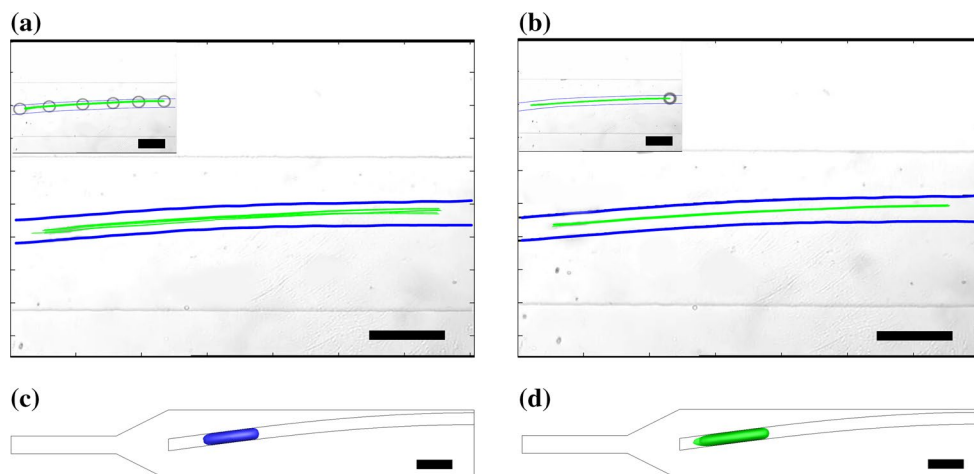
in Fig. 6c, d. In the simulations, material constants provided in Table 1 for Exp. IV and V were used. In agreement with the experimental results shown in Fig. 6a, b, no droplets are observed to be guided in Fig. 6c, while all droplets are strongly guided in Fig. 6d. In Fig. 6d, the simulated droplets are observed to be strongly deformed and flattened as they are guided along the track; this behavior was not observed in the experiments presented in Fig. 6b. This difference in the droplet behavior can be attributed to incomplete removal of PDMS from the laser-ablated tracks. In the experiments, some residues of PDMS are left on the glass surface after laser ablation. This is indicated by the roughness observed in the surface profiles of the ablated tracks shown in Fig. S2 in ESI. In order to fully characterize the presence of residual PDMS on the laser-ablated surfaces, we performed scanning electron microscopy (SEM) and Raman spectroscopy of a clean glass substrate, a PDMS substrate, and the ablated track region. The results of these experiments provided in ESI (Figs. S3–S6) clearly indicate the presence of residual PDMS on the surface of the laser-ablated sinusoidal track. Residual PDMS remaining on the track surface then renders this surface less hydrophilic which results in a higher contact angle of pure water on this surface and, consequently, lower wetting of the surface by the droplets of pure water. Thus, the size of the contact area between the droplet and the track decreases, resulting in more spherical droplets observed in the experiments, in contrast to the simulated droplet shape.

Experimental and simulated trajectories observed in Chip A for pure ethylene glycol and pure water droplets are shown in Fig. 7 (Exps. VI and VII). Pure water and pure ethylene glycol have different polarity and interfacial tension in olive oil, but they display similar contact angles on glass and PDMS when immersed in the oil (see supplementary Fig. S7). Similarity of the results obtained for pure water and pure ethylene glycol then shows that the main guiding mechanism taking place is due to the increased wettability—or reduced contact angle—in the central ablated region. The

flow rates of oil and droplet liquid in both cases were kept at 20  $\mu\text{L/h}$  and 1  $\mu\text{L/h}$ , respectively, yielding similar droplet sizes. In particular, droplet size and speed ranged between 96–106  $\mu\text{m}$  (100–117  $\mu\text{m}$ ) and 203–245  $\mu\text{m/s}$  (267–286  $\mu\text{m/s}$ ) in Fig. 7a (Fig. 7b), respectively. For both ethylene glycol and water droplets, complete guiding is observed in Fig. 7a, b. Full videos of guided droplets can be found in ESI (movies S6 and S7). These results have also been verified by the numerical simulations shown in Fig. 7c, d. Similarly to the simulation result of Fig. 6d, simulated droplets in Fig. 7c, d are observed to be deformed due to strong wetting of the guiding tracks. Such deformations were not observed in the experiments because of the residual PDMS left on the guiding track surface after the laser ablation, resulting in decreased wettability of the track surface with polar droplet liquids.

Finally, experiments with ethylene glycol/SDS droplets were carried out in chip A (Exp. VIII). In these experiments, flow rates of oil and water were kept at 20  $\mu\text{L/h}$  and 1  $\mu\text{L/h}$ , respectively. Resulting size of the droplets then varied from 96 to 103  $\mu\text{m}$ , and the speed of the droplets varied from 228 to 265  $\mu\text{m/s}$ . Experimental trajectories of the droplets are shown in Fig. 8. The contact angle of ethylene glycol/SDS droplets on a glass surface immersed in olive oil was measured to be  $51.8^\circ$ , very similar to the cases of pure water and pure ethylene glycol droplets surrounded by oil. Consequently, due to the relatively good wetting of the glass surface, ethylene glycol/SDS droplets display complete guiding, just like the droplets of pure water and pure ethylene glycol. This finding is in strong contrast with the results obtained for water/SDS droplets under similar operating conditions (droplet size and speed) as shown in Fig. 6a where no guiding is observed for water/SDS droplets. Comparison of the results obtained for both water and ethylene glycol droplets without and with the surfactant suggests that the organization of the surfactant layer at the droplet surface represents a major factor determining the stability of droplet guiding.

**Fig. 7** Droplet guiding experiments performed with **a** pure ethylene glycol and **b** pure water droplets in Chip A (Exps. VI and VII). Parts **c** and **d** show the simulation results for the experiments presented in parts **a** and **b**, respectively. All scale bars are 200  $\mu\text{m}$ . See also Movies S6, S7, S12, and S13 in ESI



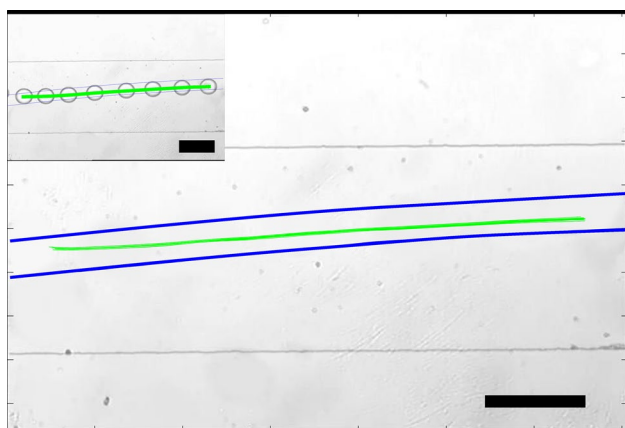


**Fig. 8** Droplet guiding experiments performed with ethylene glycol/SDS droplets. Scale bar is 200  $\mu\text{m}$ . See also Movie S8

Specifically, while the addition of the surfactant causes a dramatic change in the guiding behavior of water droplets, no such change is observed for ethylene glycol droplets upon adding the surfactant. These results also indicate that the polarity of the bulk droplet liquid plays only a marginal role in the guiding, which is almost completely controlled by the droplet interfacial energy given by the complex physico-chemical interactions between the droplet liquid, the surfactant layer, and the host medium.

#### 4 Conclusions

We have presented a comprehensive study of guiding of emulsion microdroplets along surface tracks obtained by laser ablation of PDMS films of micrometer thickness deposited on glass slides; these guiding tracks are defined by topography and wettability of the patterned surface. We have analyzed the stability of droplet guiding for different polar liquids with different interfacial properties with respect to the host liquid formed by olive oil. Following conclusions have been drawn from the results of experiments and numerical simulations:

- Experiments with water/SDS droplets moving along 1-, 1.5-, and 2- $\mu\text{m}$  deep guiding tracks revealed no guiding, partial guiding, and complete guiding, respectively, in the three considered cases. These experiments show that for constant chemical properties of the surface, surface topography plays an important role in the stability of droplet guiding, especially for track depths larger than 2  $\mu\text{m}$ . Experimental results have been verified by numerical simulations showing the presence and absence of guiding of water/SDS droplets along 2- and 1- $\mu\text{m}$  deep tracks, respectively.

- Experiments with guiding of water/SDS droplets along tracks of different depths indicate that large droplets (diameters larger than  $\sim 100 \mu\text{m}$ ) display the highest sensitivity of the confinement—characterized by the distance of the guided droplet center from the track center—to the depth of the guiding track. This is a direct result of the capacity of these bigger droplets to interact physically with both sides of the track and benefit from additional surface support. With increasing depth of the track, the differences in confinement of droplets of different sizes become more pronounced. This size dependence of the droplet confinement can be potentially used for sorting droplets with different sizes.
- Analysis of guiding of droplets of pure water, pure ethylene glycol, water/SDS, and ethylene glycol/SDS mixtures along a 1- $\mu\text{m}$  deep guiding track indicates complete guiding for water, ethylene glycol, and ethylene glycol/SDS cases and no guiding for water/SDS case. Guiding of water, ethylene glycol, and ethylene glycol/SDS droplets is ensured by their low contact angles on the glass surface immersed in oil (close to  $50^\circ$ ). In contrast, water/SDS droplets exhibit higher contact angle on glass in oil (more than  $110^\circ$ ) which prevents their efficient guiding. These experiments show that for the shallowest guiding track of 1  $\mu\text{m}$  depth, modification of the interfacial interaction energy rather than the topographical step on the surface is the main mechanism responsible for droplet guiding. This dependence of guiding stability on the interfacial energy can be potentially used for droplet sorting according to their surface energy.
- For the droplets of pure water and pure ethylene glycol moving along a 1- $\mu\text{m}$  deep track, numerical simulations have revealed stronger confinement than observed experimentally. This difference is attributed to the residual PDMS remaining on the track surface after laser ablation which results in a decreased wettability of the guiding track by polar liquids in the experiments.

The presented novel technique for surface-assisted droplet guiding along laser-ablated tracks can be exploited for passive sorting of microdroplet mixtures flowing in the same microfluidic chip based on their inherent wetting properties and/or size. This study also paves the way for autonomous solutions for integrated lab-on-a-chip biological screening, therapeutic agent delivery, diagnostic chips, drug discovery, and isolation of dissolved chemical compounds. The fact that the droplet guiding can be achieved purely on the basis of surface energy modifications can also inspire other droplet guiding schemes that would enable defining reconfigurable tracks by surface energy modifications obtained using other external control mechanisms such as electric field (Mannetje et al. 2014) or light (Lim et al. 2006).



## 5 Supporting information available

Guiding movies of exemplary droplets for all the experiments and simulations.

**Acknowledgements** This work was supported by TÜBİTAK (Grant No. 112T972). Z. Rashid and B. Morova thank HEC Pakistan and ASEL SAN A.S., respectively, for Ph.D. scholarships. The authors thank M. Waqas Nawaz and Z. Emami for help with initial experiments, A. Ijaz for help with interfacial tension measurements, and M. B. Yağcı for help with SEM and Raman measurements in Koç University Surface Science and Technology Center (KUYTAM).

## References

- Aas M, Jonáš A, Kiraz A, Brzobohatý O, Ježek J, Pilát Z, Zemánek P (2013) Spectral tuning of lasing emission from optofluidic droplet microlasers using optical stretching. *Opt Exp* 21:21380–21394
- Abbyad P, Dangla R, Alexandrou A, Baroud CN (2010) Rails and anchors: guiding and trapping droplet microreactors in two dimensions. *Lab Chip* 115:813–821
- Abbyad P, Tharaux PL, Martin JL, Baroud CN, Alexandrou A (2010) Sickling of red blood cells through rapid oxygen exchange in microfluidic drops. *Lab Chip* 10:2505–2512
- Ahn K, Kerbage C, Hunt TP, Westervelt RM, Link DR, Weitz DA (2006) Dielectrophoretic manipulation of drops for high-speed microfluidic sorting devices. *Lab Chip* 88:241041–241043
- Anslys Fluent Theory Guide (2013) vol 15.0
- Baroud CN (2014) In: Kohler JM, Cahill BP (eds) *Micro-segmented flow, applications in chemistry and biology*. Springer, Berlin, Chapter 2, pp 7–29
- Chetouani H, Jeandey C, Haguet V, Rostaing H, Dieppedale C, Reyne G (2006) Diamagnetic levitation with permanent magnets for contactless guiding and trapping of microdroplets and particles in air and liquids. *IEEE Trans Magn* 42:3557–3559
- Choi J, Son G (2008) Numerical study of droplet motion in a microchannel with different contact angles. *J Mech Sci Eng* 22:2590–2599
- Cookey GA, Obunwo CC, Uzoma DO (2015) The effect of temperature on the micellization of an anionic surfactant in mixed solvent systems. *IOSR. J Appl Chem* 8:49–54
- Dangla R, Lee S, Baroud CN (2014) Trapping microfluidic drops in wells of surface energy. *Phys Rev Lett* 107:124501-1–124501-4
- Fradet E, McDougall C, Abbyad P, Dangla R, McGloin D, Baroud CN (2011) Combining rails and anchors with laser forcing for selective manipulation within 2D droplet arrays. *Lab Chip* 11:4228–4234
- Franke T, Abate AR, Weitz DA, Wixforth A (2009) Surface acoustic wave (SAW) directed droplet flow in microfluidics for PDMS devices. *Lab Chip* 9:2625–2627
- Ganesan S (2012) On the dynamic contact angle in simulation of impinging droplets with sharp interface methods. *Microfluid Nanofluidics* 14:615–625
- Garstecki P, Fuerstman MJ, Stone HA, Whitesides GM (2006) Formation of droplets and bubbles in a microfluidic T-junction-scaling and mechanism of break-up. *Lab Chip* 6:437–446
- Gupta R, Fletcher DF, Haynes BS (2009) On the CFD modelling of Taylor flow in microchannels. *Chem Eng Sci* 64:2941–2950
- Hummer D, Kurth F, Rainer NN, Dittich PS (2016) Single cells in confined volumes: microchambers and microdroplets. *Lab Chip* 16:447–458
- Jonáš A, Yalızay B, Aktürk S, Kiraz A (2014) Free-standing optofluidic waveguides formed on patterned superhydrophobic surfaces. *Appl Phys Lett* 104:091123
- Karapetsas G, Chamakos NT, Papathanasiou AG (2016) Efficient modelling of droplet dynamics on complex surfaces. *J Phys Condens Matter* 28:8510-1–85101-16
- Lee H, Liu Y, Westervelt RM, Ham D (2006) IC/microfluidic hybrid system for magnetic manipulation of biological cells. *IEEE J Solid State Circuits* 41:1471–1480
- Lim HS, Han JT, Kwak D, Jin M, Cho K (2006) Photoreversibly switchable superhydrophobic surface with erasable and rewritable pattern. *J Am Chem Soc* 128:14458–14459
- Lim CY, Lam YC (2014) Phase field simulation of impingement and spreading of micro-sized droplet on heterogeneous surface. *Microfluid Nanofluidics* 17:131–148
- Malekzadeh S, Roohi E (2015) Investigation of different droplet formation regimes in a T-junction microchannel using the VOF technique in OpenFOAM. *Microgravity Sci Technol* 27:231–243
- Mannetje D, Ghosh S, Lagraauw R, Otten S, Pit A, Berendsen C, Zeegers J, van den Ende D, Mugele F (2014) Trapping of drops by wetting defects. *Nat Commun* 5:1–7
- Mei F (ed) (2008) *Dual capillary electrospraying—fundamentals and applications*. Pro Quest, Saint Louis, Missouri
- Menech MD, Garstecki P, Jousse F, Stone HA (2008) Transition from squeezing to dripping in a microfluidic T-shaped junction. *J Fluid Mech* 595:141–161
- Pit AM, Duits MHG, Mugele F (2015) Droplet manipulations in two phase flow microfluidics. *Micromachines* 6:1768–1793
- Rakszewska A, Tel J, Chokkalingam V, Huck WT (2014) One drop at a time: toward droplet microfluidics as a versatile tool for single-cell analysis. *NPG Asia Mater* 6:1–11
- Sidram MH, Bhajantri NU (2015) Exploration of normalized cross correlation to track the object through various template updating techniques. *IOSR J VLSI Signal Process* 5:22–35
- Teh SY, Lin R, Hung LH, Lee AP (2008) Droplet microfluidics. *Lab Chip* 8:198–220
- Than P, Preziosi L, Joseph D, Arney M (1988) Measurement of interfacial tension between immiscible liquids with the spinning rod tensiometer. *J Colloid Interface Sci* 124:552–559
- Tullis J, Park CL, Abbyad P (2014) Selective fusion of anchored droplets via changes in surfactant concentration. *Lab Chip* 14:3285–3289
- Unger MA, Chou H-P, Thorsen T, Scherer A, Quake SR (2000) Monolithic microfabricated valves and pumps by multilayer soft lithography. *Science* 288:113–116
- Wang S, Kallur A, Goshu A (2011) Fabrication and characterization of PDMS thin film
- Worner M (2012) Numerical modeling of multiphase flows in microfluidics and micro process engineering: a review of methods and applications. *Microfluid Nanofluidics* 12:841–886
- Wu L, Tsutahara M, Kim LS, Ha M (2008) Three dimensional lattice Boltzmann simulations of droplet formation in a cross-junction microchannel. *Int J Multiph Flow* 34:852–864
- Xu L, Lee H, Panchapakesan R, Oh KW (2012) Fusion and sorting of two parallel trains of droplets using a railroad-like channel network and guiding tracks. *Lab Chip* 12:3936–3942
- Yoon DH, Numakunai S, Nakahara A, Sekiguchi T, Shoji S (2014) Hydrodynamic on-rail droplet pass filter for fully passive sorting of droplet-phase samples. *RSC Adv* 4:37721–37725